




Emergent non-Hermitian modelsLumen Eek ¹, Anouar Moustaj ¹, Malte Röntgen ², Vincent Pagneux², Vassos Achilleos², and Cristiane Morais Smith¹¹*Institute of Theoretical Physics, Utrecht University, Utrecht, 3584 CC, Netherlands*²*Laboratoire d'Acoustique de l'Université du Mans, Unité Mixte de Recherche 6613, Centre National de la Recherche Scientifique, Avenue O. Messiaen, F-72085 Le Mans Cedex 9, France*

(Received 24 October 2023; accepted 15 December 2023; published 11 January 2024)

The Hatano-Nelson and the non-Hermitian Su-Schrieffer-Heeger models are paradigmatic examples of non-Hermitian systems that host nontrivial boundary phenomena. In this work, we use recently developed graph-theoretical tools to design systems whose isospectral reduction, akin to an effective Hamiltonian, has the form of either of these two models. In the reduced version, the couplings and onsite potentials become energy dependent. We show that this leads to interesting phenomena such as an energy-dependent non-Hermitian skin effect, where eigenstates can simultaneously localize on either ends of the systems, with different localization lengths. Moreover, we predict the existence of various topological edge states, pinned at nonzero energies, with different exponential envelopes, depending on their energy. Overall, our work sheds light on the nature of topological phases and the non-Hermitian skin effect in one-dimensional systems.

DOI: [10.1103/PhysRevB.109.045122](https://doi.org/10.1103/PhysRevB.109.045122)**I. INTRODUCTION**

In recent years, the study of non-Hermitian physics has gained significant attention due to its profound impact on the fields of condensed matter, metamaterials, acoustics, and photonics [1–4]. Indeed, non-Hermitian platforms offer enhanced sensing capabilities [1], can exhibit Majorana bound states near exceptional points [2], and provide opportunities for utilizing topological edge modes in the field of active matter [3,4]. In addition, the nonconservative and nonunitary dynamics of non-Hermitian systems have led to the discovery of phenomena that challenge the conventional notions of symmetry and stability [5–8]. Among these, the non-Hermitian skin effect (NHSE), manifesting itself as an accumulation of modes at the boundaries of the system, has been intensely studied in the past few years [9–14]. The NHSE has been realized in multiple platforms, such as acoustic crystals [12], electric circuits [13], and optical lattices using ultracold atoms [15]. Moreover, the interplay between non-Hermitian physics and topology has given rise to novel topological phases [7,16–18]. Indeed, when considering Hamiltonians that are no longer Hermitian [7,19], the Altland-Zirnbauer topological classification for noninteracting fermions is enlarged from 10 to 38 classes. Additionally, the bulk-boundary correspondence generally no longer holds, and requires substantial modifications to account for boundary phenomena [5,20].

The investigation of toy models has been instrumental in shaping a theoretical comprehension of non-Hermitian systems. The Hatano-Nelson and the non-Hermitian Su-Schrieffer-Heeger (NH SSH) models [21–23], for instance, have become paradigmatic examples of systems hosting the NHSE and a non-Bloch bulk-boundary correspondence, respectively. Upon departing from these idealized models, the same phenomena may take place, but may be more difficult to describe. One way to bridge this difficulty is to reduce the complicated problem into one described by simpler models,

with additional features revealed through the reduction process.

An interesting technique, originally introduced for the analysis of graphs and network models, that may be used for this purpose is the so-called isospectral reduction (ISR) [24]. The idea behind the ISR is to reduce the matrix dimensionality while preserving the spectrum of the original Hamiltonian H . This is achieved by recasting the original linear eigenvalue problem into a nonlinear one. The reduced dimensionality simplifies certain tasks and may, in particular, reveal hidden structures of the system [25]. Pivoting around this favorable properties, the ISR has been applied to different problems, for instance, to yield better eigenvalue approximations [26] or to study pseudospectra of graphs and matrices [27]. In physics, the ISR is often encountered in the form of an effective Hamiltonian. One example of this is the Brillouin-Wigner perturbation theory, where the partitioning is done in terms of degenerate subspaces of an unperturbed Hamiltonian [28]. Another example would be integrating out degrees of freedom, where the partitioning is done in Fock space, or integrating out high momentum modes [29]. In that context, the reduction provides a suitable starting point for perturbation theory. In the treatment of open systems, for example, scattering problems, the ISR is similar to a Feshbach-Fano partitioning [30].

In the last few years, the ISR has also been applied to uncover hidden, so-called latent, symmetries [31].¹ Latent symmetries become apparent after reduction and have been

¹We note that it has recently been shown [32] that the concept of latent symmetry is, for the special case of latent reflection symmetries, equivalent to the graph-theoretical concept of cospectrality [33]. A good overview over the properties of cospectrality is given in Chap. 3 of [34].

studied in a number of applications, including quantum information transfer [35], the design of lattices with flat bands [36] or the explanation of accidental degeneracies [37]. Very recently, latent symmetries have also been explored in waveguide networks [38,39], including a possible application in secure transfer of information [40].

In this work, we propose to apply the ISR to a range of one-dimensional (1D) non-Hermitian tight-binding models, such that they reduce to the paradigmatic Hatano-Nelson and the NH SSH models. This method allows us to predict the existence of various topological phases and nonstandard NHSE as well as to uncover various properties, which were hitherto still unexplored. As an example of the unusual characteristics of this class of models, our approach reveals that they exhibit an energy- (or frequency-) dependent NHSE, where eigenstates can localize on either end of the systems. The degree of localization of the NHSE is also influenced by this energy dependence. A similar behavior was recently observed in a system of coupled ring resonators [41,42], for which we extend the theoretical understanding. In addition, we find various topological states pinned at different nonzero energies, protected by a latent spectral symmetry that is only revealed upon applying the ISR. As a consequence of this energy dependence, their exponential envelopes vary, a feature that is also straightforwardly explained, and predicted, upon using the ISR. Throughout this work, we restrict our attention to systems from which the Hatano-Nelson [21] and the NH SSH [22,23] models emerge. It should be noted that one could also engineer other types of systems, from which different models would emerge through the ISR. Indeed, the special case of an asymmetric, Hermitian system from which the conventional SSH model emerges, has been very recently demonstrated [43].

This paper is structured as follows: In Sec. II, we lay down the main tool used for the analysis of our models. That is, the ISR, which amounts to the construction of an effective Hamiltonian model that is already well understood. This is used on a minimal example, where we do not *a priori* expect nonreciprocity to be present. The ISR allows for an intuitive understanding of the reason why the NHSE would arise in such a setup. In Sec. III, we extend our analysis to a slightly more complex case, and apply the ISR to a quasi-one-dimensional system, resulting in an “emergent” Hatano-Nelson model [21]. In this setup, we are able to predict the existence of an energy-dependent NHSE. In Sec. IV, we add a connection between the unit cells that leads to an “emergent” NH SSH model [23], from which a full understanding of the topological phases can be drawn. In Sec. V, we generalize the construction principle for which the analysis done for the previous models can be applied. Finally, in Sec. VI, we conclude by summarizing our results.

II. ISOSPECTRAL REDUCTION

Given a Hamiltonian H , it is possible to partition a choice of basis into a set S and its complement \bar{S} , so that H can be written in block form as

$$H \equiv \begin{pmatrix} H_{S,S} & H_{S,\bar{S}} \\ H_{\bar{S},S} & H_{\bar{S},\bar{S}} \end{pmatrix}. \quad (1)$$

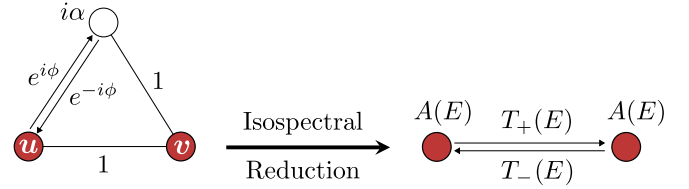


FIG. 1. Isospectral reduction of the lossy, complex hopping model on the left to the red sites $S = \{u, v\}$ yields the nonreciprocal effective model on the right. Circles denote sites, and lines denote couplings.

By partitioning the eigenvalue problem $H|\psi\rangle = E|\psi\rangle$ [where $|\psi\rangle \equiv (|\psi_S\rangle, |\psi_{\bar{S}}\rangle)^T$] into the different subsets S and \bar{S} and subsequently eliminating $|\psi_{\bar{S}}\rangle$, we obtain the nonlinear eigenvalue problem

$$\mathcal{R}_S(E, H)|\psi_S\rangle = E|\psi_S\rangle. \quad (2)$$

Here,

$$\mathcal{R}_S(E, H) = H_{S,S} - H_{S,\bar{S}}(H_{\bar{S},\bar{S}} - E\mathbb{1})^{-1}H_{\bar{S},S} \quad (3)$$

is the effective Hamiltonian for the subsystem S .² In the language of graph theory, $\mathcal{R}_S(E, H)$ is known as the ISR of H to S [24]. An overview of the application of the ISR to physical systems is given in Ref. [44].

In this work, we show how the ISR allows us to understand the behavior of systems without making approximations. This is done by recognizing that the ISR of a system may yield another (energy-dependent) known model, which is well understood. In this case, the properties of the known reduced system can be used to make predictions for the full system. However, it should be emphasized that the energy-dependent parameters that result from this construction are not truly physical. We shall now illustrate this by means of a simple but important example.

A conventional and intuitive reason for the NHSE to appear is understood through the lens of nonreciprocity. An exemplary illustration of this phenomenon can be found in the Hatano-Nelson model [21]. Alternatively, the NHSE can be induced by a combination of onsite gain or dissipation and complex couplings, but this mechanism may appear less intuitive [45]. Consider the system depicted on the left-hand side of Fig. 1. It is a three-site non-Hermitian tight-binding Hamiltonian, with complex hopping parameters and one site featuring an imaginary onsite term. Specifically, if we enumerate the sites such that u, v are the first two, the Hamiltonian is given by

$$H = \begin{pmatrix} 0 & 1 & e^{i\phi} \\ 1 & 0 & 1 \\ e^{-i\phi} & 1 & i\alpha \end{pmatrix}.$$

Through an ISR to the red sites, the resulting effective model on the right-hand side is obtained. This reduced model exhibits a new onsite potential and hopping amplitudes, given

²Chapter 5.8.3 of G. Grosso and G.P. Parravicini, *Solid State Physics*, 2nd ed. (Academic, New York, 2014).

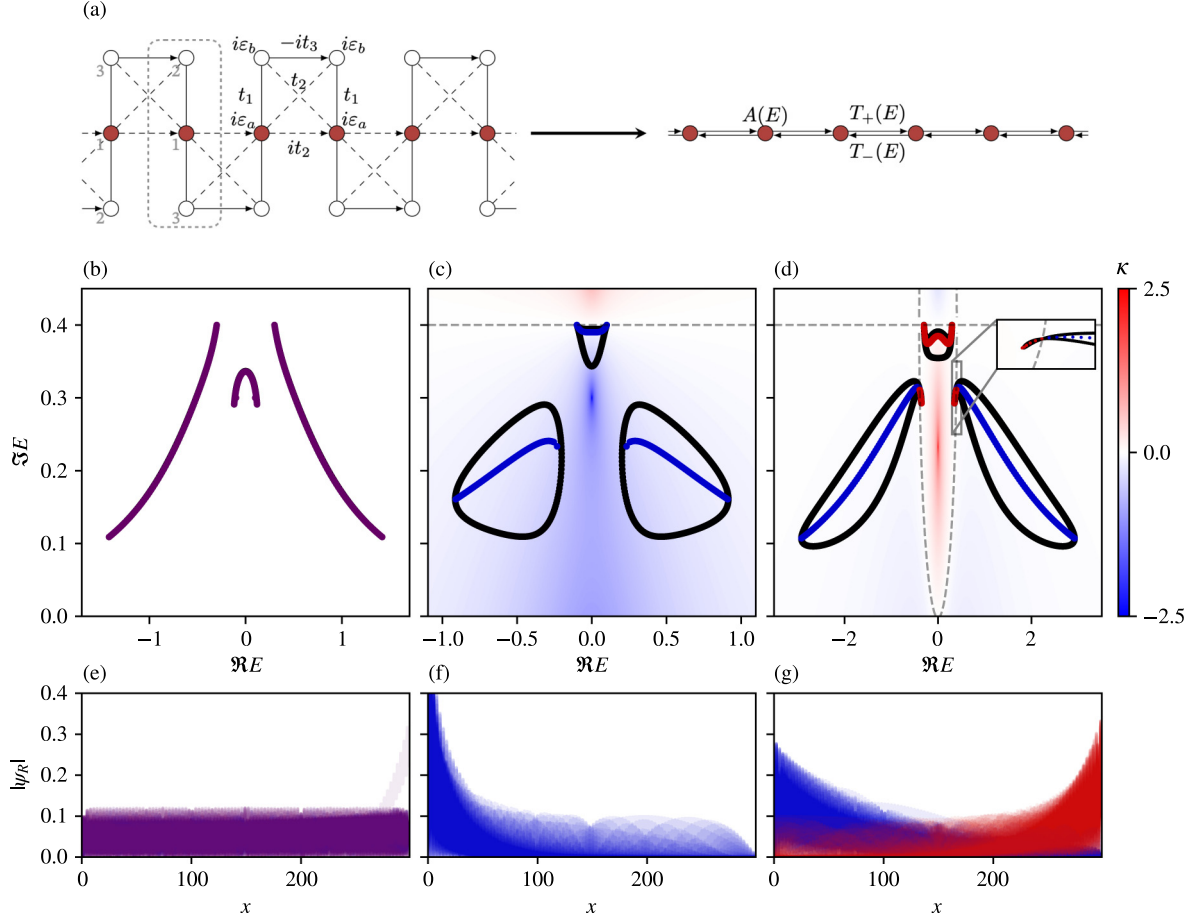


FIG. 2. Emergent Hatano-Nelson model from ISR. (a) Lattice corresponding to the Bloch Hamiltonian given in Eq. (4) and its ISR to the Hatano-Nelson model with energy-dependent hopping and an energy-dependent onsite term. The unit cell of the left chain is indicated by the gray dashed lines and the sites are labeled. (b)–(d) The complex energy spectra are presented for the system described in (a) using different parameter values: (b) $(\varepsilon_a, \varepsilon_b, t_1, t_2, t_3) = (0, 0.4, 0, 0.5, 0.3)$; (c) $(\varepsilon_a, \varepsilon_b, t_1, t_2, t_3) = (0, 0.4, 0.4, 0.2, 0.1)$; and (d) $(\varepsilon_a, \varepsilon_b, t_1, t_2, t_3) = (0, 0.4, 0.4, 1, 0.3)$. The dots are color coded, representing left-localized (blue), right-localized (red), or bulklike (purple) modes, with black and colored lines indicating PBC and OBC, respectively. The background displays $\kappa(E)$, where larger absolute values of κ indicate stronger localization of the corresponding skin mode. Dashed gray lines correspond to $\kappa(E) = 0$. (e)–(g) Right eigenstates are shown for the same parameter choices as the above panels, using the same coloring conventions.

by

$$A(E) = \frac{1}{E - i\alpha},$$

$$T_{\pm}(E) = 1 + \frac{e^{\pm i\phi}}{E - i\alpha},$$

respectively. Notice how the hopping displays asymmetry in its magnitude, i.e., $|T_+(E)| \neq |T_-(E)|$, thereby indicating nonreciprocity within the model, in the same way as the Hatano-Nelson model. By employing an ISR, both avenues for realizing the NHSE, either directly by nonreciprocal couplings, or through reciprocal couplings but non-Hermitian onsite potentials, can be unified.

In the following sections, we will modify our prototypical model slightly in order to have interesting and emergent phenomena taking place. By considering a one-dimensional chain of fully connected four-site models instead of three-site ones, like in Fig. 1, we are able to obtain an energy-dependent skin effect that induces localization on both sides of the system.

III. EMERGENT HATANO-NELSON MODEL

Let us consider the model depicted in Fig. 2(a). Taking the unit cell as indicated in the figure, the Bloch Hamiltonian of this lattice is given by

$$H(k) = \begin{pmatrix} i\varepsilon_a - 2t_2 \sin k & t_1 + t_2 e^{-ik} & t_2 + t_1 e^{-ik} \\ t_1 + t_2 e^{ik} & i\varepsilon_b & it_3 \\ t_2 + t_1 e^{ik} & -it_3 & i\varepsilon_b \end{pmatrix}. \quad (4)$$

Here t_1 , t_2 , and t_3 are real-valued hopping parameters, ε_a and ε_b are onsite gains or losses, and k is the wave vector. Furthermore, we have set the lattice spacing to be equal to unity.

We note at this point that the spectrum has a mirror symmetry with respect to the $\text{Re}(E) = 0$ line; cf. Figs. 2(b) to 2(d). The mirror-symmetric spectrum stems from the fact that

$$SH(k)S^{-1} = -H^*(-k),$$

$$S = (-\sigma_z) \oplus 1, \quad (5)$$

where σ_z acts on the two sites of the unit cell. In the literature, this symmetry is better-known as PHS[†] [7], which is one of the two nonequivalent realizations of particle-hole symmetry in a non-Hermitian system.

If we simultaneously perform an ISR to all red sites of the full lattice, and take the Bloch-Hamiltonian of the resulting effective model, we obtain

$$H_R(k, E) = A(E) + T_+(E)e^{ik} + T_-(E)e^{-ik}, \quad (6)$$

in which we recognize the Hatano-Nelson model with energy-dependent onsite term $A(E)$, and hopping parameters $T_{\pm}(E) \equiv v(E) \pm g(E)$.³ Here

$$\begin{aligned} A(E) &= i \left[\varepsilon_a + \frac{2(\varepsilon_b + iE)(t_1^2 + t_2^2)}{(\varepsilon_b + iE)^2 + t_3^2} \right], \\ v(E) &= 2i \frac{(\varepsilon_b + iE)t_1 t_2}{(\varepsilon_b + iE)^2 + t_3^2}, \\ g(E) &= i \frac{t_2 t_3 (t_3 - t_2) + t_2 (\varepsilon_b + iE)^2 + t_1^2 t_3}{(\varepsilon_b + iE)^2 + t_3^2}. \end{aligned} \quad (7)$$

For the ordinary Hatano-Nelson model, i.e., no energy-dependent parameters, it is well known that the NHSE is present when $|T_+| \neq |T_-|$ [6,21]. This condition still holds for our effective Hamiltonian. After some algebraic manipulations, it can be expressed as

$$v_R(E)g_R(E) + v_I(E)g_I(E) \neq 0. \quad (8)$$

Here, the subscripts R and I represent real and imaginary part, respectively. By substituting Eq. (7) into Eq. (8), it follows that the NHSE is present when t_1 , t_2 , and ε_b are all nonzero (see Appendix A).

Let us now visualize the above statements in terms of the eigenvalues and eigenstates. We start by inspecting a setup with $t_1 = 0$ and show its eigenvalue spectrum in Fig. 2(b). The spectrum (denoted by a solid purple line) is the same for open boundary conditions (OBC) and periodic boundary conditions (PBC). The (right) eigenvectors are depicted in Fig. 2(e) and show, as expected, no NHSE. However, upon close inspection of Fig. 2(e), one can see a mode sitting at the right boundary. This is a consequence of lattice termination and is elaborated upon in Sec. V A.

Leaving the trivial case behind us, we next investigate a setup where t_1 , t_2 , and ε_b are all nonzero. Specifically, we choose $(\varepsilon_a, \varepsilon_b, t_1, t_2, t_3) = (0, 0.4, 0.4, 0.2, 0.1)$. For this choice of parameters, the eigenvalue spectrum is shown in Fig. 2(c). The black line represents the PBC eigenvalue spectrum, which forms three simple loops in the complex energy plane. Importantly, the PBC spectrum now no longer coincides with the OBC spectrum (shown in blue). The background color in this figure represents a contour plot of the skin

length scale [6]

$$\kappa(E) \equiv \log \sqrt{\left| \frac{T_-(E)}{T_+(E)} \right|}. \quad (9)$$

We note that κ is energy dependent, which is a consequence of the energy dependence of the system's hopping parameters. This energy dependence is an important difference to the ordinary Hatano-Nelson model. There, κ is constant, such that all skin modes show the same length scale. In an emergent Hatano-Nelson model, on the other hand, each mode has its own skin length given by Eq. (9). In particular, a (right) PBC eigenstate whose energy E lies in a region with $\kappa < 0$ ($\kappa > 0$) will be localized at the system's left (right) boundary. Now, since all of the system's OBC eigenvalues correspond to $\kappa < 0$, we expect all of the eigenstates to be left localized. This is indeed the case, as can be seen from Fig. 2(f).

Let us now modify the parameters to realize the so-called bipolar NHSE [46]. A system with a bipolar NHSE features two classes of right eigenstates: one being localized at the left boundary, and the other localized at the right boundary. To find this phenomenon in our setup, we choose $(\varepsilon_a, \varepsilon_b, t_1, t_2, t_3) = (0, 0.4, 0.4, 1, 0.3)$. The system's eigenvalues are depicted in Fig. 2(d), which has an insectlike shape. Again, PBC (black) and OBC (blue and red) spectra do not coincide, as expected from the fact that all t_1 , t_2 , and ε_b are nonvanishing. What is interesting here is that $\kappa(E)$ can now take both positive and negative values. In particular, we see that Fig. 2(d) splits into two regions: an outer, blue region, where $\kappa < 0$, and an inner, red region, where $\kappa > 0$. These two regions are separated by the dashed-gray line that represents $\kappa(E) = 0$. Now, since the OBC spectrum lies both in the inner and the outer region, our system features a bipolar NHSE: (right) eigenstates whose energy E lies in the blue region are left localized, while eigenstates with E lying in the red region are right localized. This is demonstrated in Fig. 2(g), where we show the system's right eigenstates, with blue and red color corresponding to the region in which the respective eigenvalue lies.

The use of ISR does not limit itself to making predictions on the NHSE. On the contrary, it may also be used to explore topological properties of a given system. To illustrate this feature, we turn our attention to a different, but related, model in the next section.

IV. EMERGENT NON-HERMITIAN SSH MODEL

In this section, we study the system depicted in Fig. 3(a), which is a modified version of the Creutz ladder [47]. Each square forms a unit cell, interconnected by a real hopping parameter w , making this a four-band model. The momentum-space Hamiltonian for this system is given by

$$H(k) = \begin{pmatrix} i\varepsilon_a & t_1 & t_2 & it_2 + we^{-ik} \\ t_1 & i\varepsilon_b & -it_3 & t_2 \\ t_2 & it_3 & i\varepsilon_b & t_1 \\ -it_2 + we^{ik} & t_2 & t_1 & i\varepsilon_a \end{pmatrix}, \quad (10)$$

where all parameters are real valued. The setup is similar to the one used by Lee [9] to show the existence of an anomalous edge state. Our model was chosen such that its ISR to the red sites in Fig. 3(a) results in an energy-dependent NH SSH

³Unlike the original HN model, the model presented here lacks PT symmetry due to the presence of different gains and losses. As a consequence, imaginary gauge transformations into Hermitian models, as presented in Ref. [11], cannot be applied.

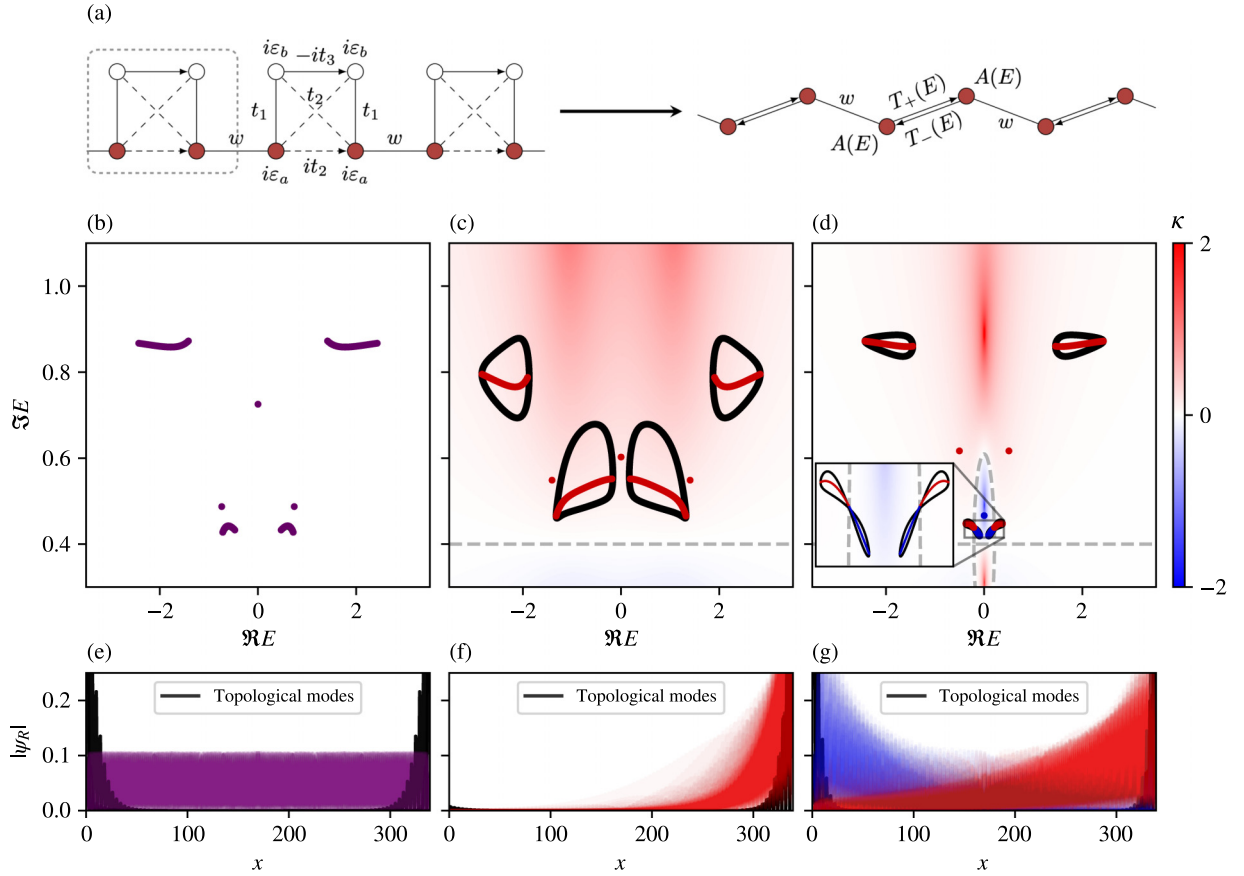


FIG. 3. Emergent NH SSH model from ISR. (a) Lattice corresponding to the Bloch Hamiltonian given in Eq. (10) and its ISR to the NH SSH model with energy-dependent hopping and an energy-dependent onsite term. (b)–(d) The complex energy spectra are presented for the system described in (a) using different parameter values: (b) $(\varepsilon_a, \varepsilon_b, t_1, t_2, t_3) = (0.9, 0.4, 0, 0.5, 0.6)$; (c) $(\varepsilon_a, \varepsilon_b, t_1, t_2, t_3) = (0.9, 0.4, 1, 0.5, 0.9)$; and (d) $(\varepsilon_a, \varepsilon_b, t_1, t_2, t_3) = (0.9, 0.4, 0.2, 0.5, 0.2)$. In all figures we take $w = 1.8$. The dots are color coded, representing left-localized (blue), right-localized (red), or bulklike (purple) modes, with black and colored lines indicating PBC and OBC, respectively. The background displays $\kappa(E)$, where larger absolute values of κ indicate stronger localization of the corresponding skin mode. Dashed gray lines correspond to $\kappa(E) = 0$. (e)–(g) Right eigenstates are shown for the same parameter choices as the above panels, using the same coloring conventions. We also plot the isolated topological modes in black.

model [22,23], described by the following Bloch Hamiltonian:

$$H_R(k, E) = \begin{pmatrix} A(E) & T_+(E) + we^{-ik} \\ T_-(E) + we^{ik} & A(E) \end{pmatrix}. \quad (11)$$

Here

$$A(E) = i \left[\varepsilon_a + \frac{(\varepsilon_b + iE)(t_1^2 + t_2^2)}{(\varepsilon_b + iE)^2 + t_3^2} \right] \quad (12)$$

and $T_{\pm}(E)$ are the same as given in Eqs. (6) and (7). This reduction is graphically depicted in Fig. 3(a). We observe that our model features a rich variety of phases, from the NHSE to topological edge modes. We note that this model enjoys the same PHS[†] symmetry as the previous three-band model, Eq. (5). However, \mathcal{S} now must be built from a different partitioning and is given by $\mathcal{S} = (-\sigma_z) \oplus \mathbb{1}_{2 \times 2}$.

A. Onset of the NHSE

Similar to the Hatano-Nelson model, the NHSE is present in the NH SSH model whenever $|T_+| \neq |T_-|$. By analogy, for our emergent NH SSH model, this results in the constraint equation $v_R(E)g_R(E) + v_L(E)g_L(E) \neq 0$. In terms of

the model parameters, this leads to the condition that the NHSE is present when t_1, t_2 , and ε_b are not equal to zero. This is illustrated in Fig. 3, where the three possible scenarios are depicted. First, Fig. 3(b) shows the case without skin effect, clearly indicated by similar band structures for OBC and PBC, and the corresponding right eigenstate in Fig. 3(e). Figure 3(c) shows the band structure when the skin effect is present, but only in one direction, as indicated by $\kappa(E) > 0$. The modes localize on the right-hand side, as shown in Fig. 3(f). Finally, Fig. 3(d) shows the band structure when the bipolar skin effect is present, which can be understood from the contour plot of $\kappa(E)$, showing both regions of $\kappa > 0$ (red) and $\kappa < 0$ in blue. In all three situations, one can observe the presence of six topological edge modes, coming in three pairs of two degenerate modes pinned at the same energy. These are shown in black in Figs. 3(e)–3(g). We will now investigate the properties of these topological modes.

B. Topological edge modes

Interestingly, we can also predict the existence of topological edge modes in the four-band model using the reduced

NH SSH chain. The winding number that determines the topological phase transition for a sublattice-symmetric 1D Hamiltonian (of which the NH SSH is an example) is given by [7]

$$\mathcal{W} = \int_{-\pi}^{\pi} \frac{dk}{4\pi i} \text{Tr} \left[\sigma_z H^{-1}(k) \frac{dH(k)}{dk} \right]. \quad (13)$$

In our case, this expression becomes energy dependent and is only applicable when

$$A(E) = E, \quad (14)$$

where $A(E)$ is defined in Eq. (12). This is because Eq. (13) is only well defined for sublattice-symmetric systems, which in our case is a latent symmetry appearing at energies satisfying Eq. (14). This means that we must consider a Hamiltonian $\tilde{H}(k) \equiv H(k, E_t) - E_t \mathbb{1}_{2 \times 2}$, where E_t is a solution of Eq. (14). For every energy satisfying this constraint, in the topological phase, there is a degenerate pair of edge states pinned at that energy. In fact, the pair is quasidegenerate, as a consequence of the finite size of the lattice. For the model at hand, there are three energies at which the transition takes place because Eq. (14) has three solutions. Explicit calculations of this winding number (see Appendix A for an analytic derivation) lead to

$$\mathcal{W}(E_t) = \begin{cases} 0, & \text{if } |w| < \sqrt{|v^2(E_t) - g^2(E_t)|} \\ 1, & \text{if } |w| > \sqrt{|v^2(E_t) - g^2(E_t)|}. \end{cases} \quad (15)$$

Substituting the solutions E_t into Eq. (15) yields the three critical values w_c at which pairs of topological edge modes appear. Figures 4(a) and 4(b) show the real and imaginary parts of the energy spectrum, respectively. The horizontal dashed lines show the calculated absolute values of the complex transition energies $E_t^{(j)} = E_R^{(j)} + E_I^{(j)}$, while the vertical dashed lines indicate the value of the predicted critical hopping parameter w_c . Robust boundary modes that persist beyond the transition point are visible in red, green, and blue. The presence of these modes can be quantified by calculating the winding number given by Eq. (15), as shown in Fig. 4(c). There is a clear jump to $\mathcal{W}(E_t) = 1$ when the critical hopping w_c is reached. Figures 4(d)–(f) show the corresponding edge states, with the same color coding, at $w = 3$. The values of the calculated transition energies E_t are indicated in the middle of each figure. Notice that to properly visualize the edge modes in the presence of the NHSE, $\sqrt{|\psi_L^* \psi_R|}$ is plotted rather than $|\psi_R|$. Moreover, it is important to highlight that, for each transition energy, the emergent sublattice symmetry of the reduced model ensures that the edge modes appear in pairs. This is visible in Figs. 4(d)–4(f), where a pair of edge states is shown for each energy E_t . For a further investigation of the line-gap closings of the emergent NH SSH model, we refer the reader to Appendix B. As a final note, we see that the penetration depth of these edge states is also energy dependent, and is given by [5,6]

$$\xi_L(E) = \frac{1}{\log \left| \frac{v(E) - g(E)}{w} \right|}, \quad (16)$$

$$\xi_R(E) = \frac{1}{\log \left| \frac{v(E) + g(E)}{w} \right|},$$

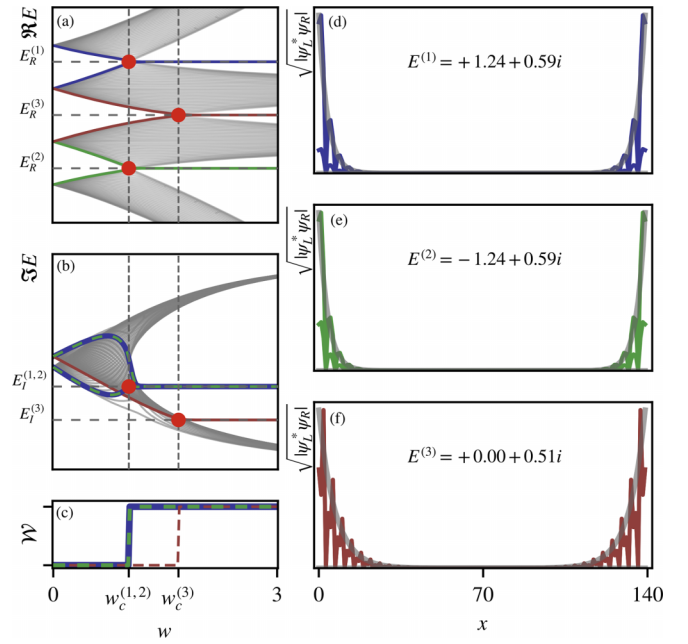


FIG. 4. Topological phase transitions of the emergent NH SSH model as a function of w . (a) Real and (b) imaginary parts of the energy spectrum, for an open chain consisting of $N_c = 35$ unit cells. The spectra are taken for the parameter choice $(\varepsilon_a, \varepsilon_b, t_1, t_2, t_3) = (0.9, 0.4, 1, 0.5, 0.6)$. (c) The winding number given by Eq. (13), calculated at the three special energies E_t , clearly shows its quantization and the critical points w . (d)–(f) Corresponding topological edge modes, at $w = 3$, plotted together with the calculated exponential envelope in gray, with penetration depth given by Eq. (17). The three different colors blue, green, red are used consistently to mark the different edge modes [(d)–(f)], the behavior of their energies [(a) and (b)], and the values of the corresponding winding number (c).

where the subscript L (R) stands for left (right) eigenvectors. This explains the different localization lengths observed in Figs. 4(d)–4(f). In the biorthogonal formulation the exponential envelope follows $\exp -x_j/2\xi_{LR}$, where $x_j = ja$ and

$$\xi_{LR} = \frac{\xi_L + \xi_R}{\xi_R \xi_L}. \quad (17)$$

This envelope is plotted in gray alongside the edge states in Figs. 4(d)–4(f).

An energy-dependent localization length is an interesting phenomenon, which is known to occur in disordered models. However, in our case it happens as a result of the non-Hermiticity and of the topological properties, which inherit an energy dependence from the parameters of the effective model, obtained through the ISR.

V. GENERALIZED CONSTRUCTION PRINCIPLES

The models treated in the previous sections are individual examples of setups whose ISR has the form of an effective Hatano-Nelson or NH SSH model. In the following, we will show that one can systematically construct large families of such systems. The procedure will always be the same: an individual unit cell is built, such that its ISR to two specific sites yields equal onsite potentials, and nonreciprocal hoppings

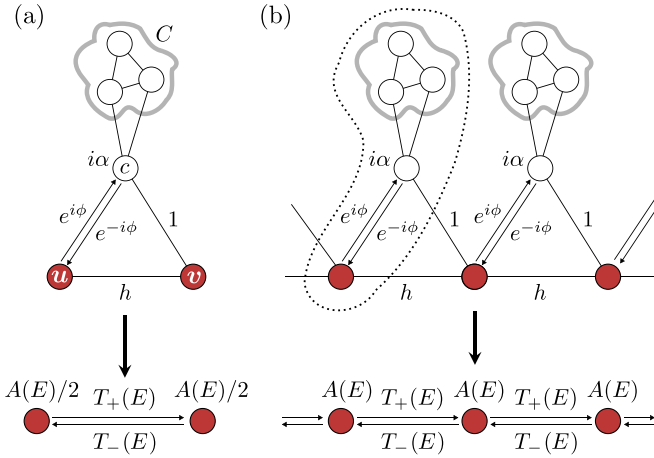


FIG. 5. (a) ISR of the lossy, complex hopping model above onto the red sites yields the nonreciprocal effective model below. (b) Lattice realization of (a). The unit cell is marked by a dashed line.

between them. Subsequently, these unit cells are connected such that either (i) a Hatano-Nelson, or (ii) a NH SSH model is obtained.

A. Emergent Hatano-Nelson models

1. Construction principle A

The starting point for the first construction principle is a finite structure that has a nonreciprocal ISR. The graphical representation of the model is sketched in Fig. 5(a). The system consists of two lower sites u and v (marked in red), which are connected to a third site c via Hermitian couplings $\exp(i\phi)$ and 1 . The site c has complex onsite potential $i\alpha$ and is further coupled to a (possibly very large) network C . For simplicity, we demand that the couplings in the network C , as well as the couplings between this network and the site c , are real valued. However, the sites in C could have complex onsite potentials. Denoting the Hamiltonian of the resulting total system by H , its ISR to the two sites u and v yields (see Appendix C)

$$\mathcal{R}_S(E, H) = \begin{pmatrix} A(E)/2 & T_+(E) \\ T_-(E) & A(E)/2 \end{pmatrix}.$$

Note that the exact form of $A(E)$ depends on the details of the network C .

This finite building block is now used to construct a lattice, as shown in Fig. 5(b), with the unit cell comprised of one site c , one network C , and one of the two red sites. Applying the ISR to all red sites, a Hatano-Nelson model emerges, as depicted in the lower part of Fig. 5(b). Importantly, since each red site of the lattice is coupled to two clouds, its onsite potential after the ISR now reads as $2A(E)/2 = A(E)$. In an open chain, the sites on the left and right end, however, will have an onsite potential of $A(E)/2$.⁴

⁴We note that this is the reason why the nontopological edge states, as seen in Fig. 2(e), appear.

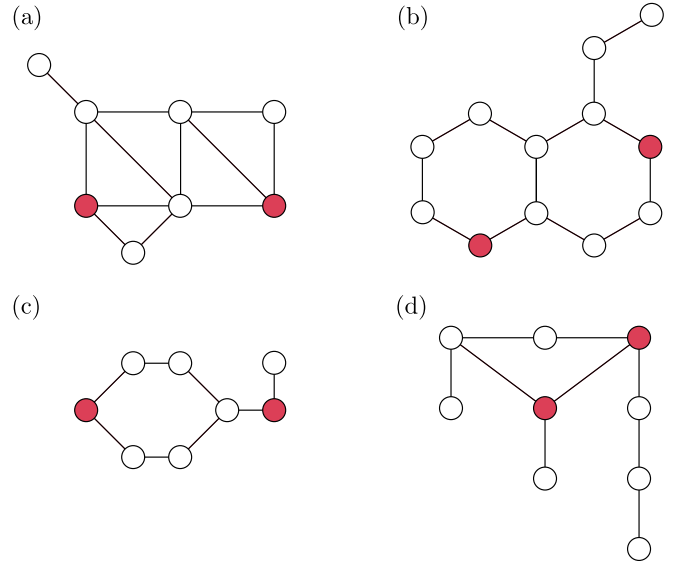


FIG. 6. Different systems with latently symmetric sites (marked in red). In all four systems, each line corresponds to a coupling of strength one (see Refs. [35,48] for more details regarding the design of latently symmetric setups).

2. Construction principle B

The second construction principle of emergent Hatano-Nelson models relies on the concept of latent symmetry [31]. Given a system G , two sites $S = \{u, v\}$ are latently reflection symmetric if the ISR over them has the form

$$\mathcal{R}_S(E, G) = \begin{pmatrix} \mathcal{A}(E) & \mathcal{B}(E) \\ \mathcal{B}(E) & \mathcal{A}(E) \end{pmatrix}, \quad (18)$$

that is, if $\mathcal{R}_S(E, H)$ commutes with the permutation matrix $P := \sigma_x$. In Fig. 6, a number of setups with latently symmetric sites (marked in red) are shown. A broader overview over this topic is given in Ref. [44].

The construction scheme is sketched in Figs. 7(a)–7(c). Figure 7(a) depicts a real-symmetric subsystem G (marked by a cloud) in which two sites u and v (marked in blue) are latently symmetric. In other words, if one would perform the ISR over u, v , one would obtain Eq. (18). The key here is that the latent symmetry guarantees the existence of a matrix Q that commutes with the subsystem, i.e., $QG = GQ$, and which (i) permutes the sites u and v , (ii) is block diagonal, and (iii) fulfills $Q^{-1} = Q^T = Q$ [37]. In the following, we shall use this matrix extensively.

In the next step, this subsystem is modified by adding complex onsite potentials $i\epsilon$ to u and v , which are then connected via Hermitian hoppings it_3 . Note that this breaks the latent symmetry: If we denote the resulting modified subsystem by G' , then the isospectral reduction of G' over u, v would read as

$$\mathcal{R}_S(E, G') = \begin{pmatrix} \mathcal{A}(E) + i\epsilon & \mathcal{B}(E) + it_3 \\ \mathcal{B}(E) - it_3 & \mathcal{A}(E) + i\epsilon \end{pmatrix},$$

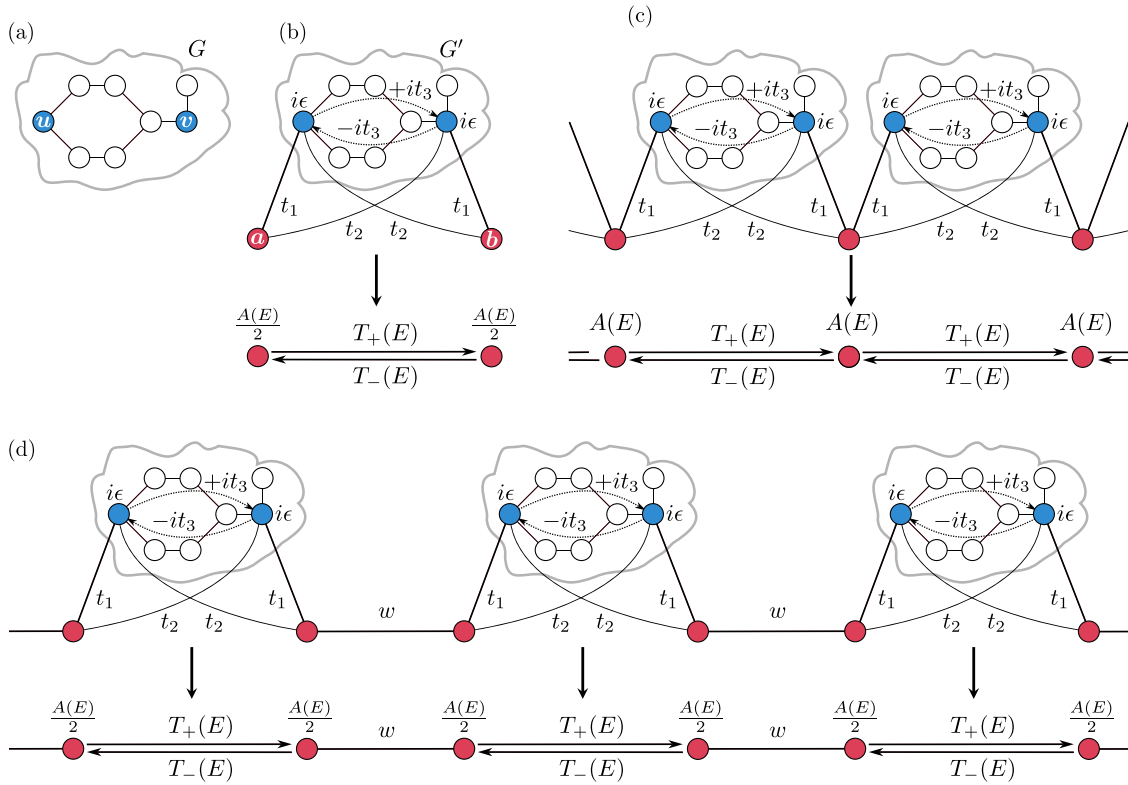


FIG. 7. Construction scheme for the emergent Hatano-Nelson and NH SSH models. (a) The starting point: a simple setup with latently symmetric sites u, v . (b)–(d) ISR of the lossy, complex hopping model above onto the red sites yields the nonreciprocal effective model below.

which does not commute with P . However, we have $\mathcal{R}_S(E, H)P = P\mathcal{R}_S(E, H)^T$. Due to the favorable properties of Q , in particular, its block-diagonal form, it can be shown that $QG' = G'^TQ$.

At this point, two additional sites a and b (marked in red) are coupled to the subsystem G' with hoppings t_1 and t_2 . Again employing the favorable properties of Q , it can be easily shown that the Hamiltonian H , describing the total system depicted in Fig. 7(b), obeys $Q'H = H^TQ'$. Here, the matrix $Q' = P \oplus Q$, with the permutation matrix P acting on the two red sites a and b . Analogously, it can be shown that the ISR has the form

$$\mathcal{R}_S(E, H) = \begin{pmatrix} A(E)/2 & T_+(E) \\ T_-(E) & A(E)/2 \end{pmatrix}.$$

Note that one can relate $A(E), B(E)$ to $A(E), T_{\pm}(E)$, though we omit the exact relation here.

Again, a lattice can be built by taking one red site and one subsystem G' as a unit cell [see Fig. 7(c)]. Taking the ISR to all red sites of this lattice doubles the onsite potential, which then becomes $A(E)$ instead of $A(E)/2$.

B. Emergent NH SSH model

In the previous Sec. V A 1, lattices were built by taking one red site and one subsystem G' as a unit cell, which resulted in emergent Hatano-Nelson models. One could, however, also

build a lattice by taking one subsystem G' and two red sites as a unit cell, and then connect neighboring unit cells via an additional coupling w , as shown in the upper part of Fig. 7(d). This results in an emergent NH SSH model, which is depicted in the lower part of Fig. 7(d). Note that, by removing all complex couplings and onsite potentials, one would obtain an effective version of the conventional SSH model. Such emergent SSH models have been very recently investigated in Ref. [43].

Before concluding this work, we investigate a specific realization of the above procedure that results in an emergent NH SSH model. The setup and its ISR are depicted in Fig. 8(a). The resulting OBC (red and blue) and PBC (black) spectra are shown in Figs. 8(b) and 8(c), where the intercell hopping parameter is $w = 2.5$ in (b) and $w = 6.5$ in (c). This leads to the appearance of 6 topological edge states in (b), and 18 in (c) (two doubly degenerate modes per energy). The overlaid transparent green circles indicate the presence of these edge modes in the OBC spectrum. The right eigenstates corresponding to the parameter choice in (b) are shown in Fig. 8(d). There, one can again observe the energy-dependent skin effect. Figures 8(e)–(g) show all six edge states that exist in (b), and their corresponding energies. Note that since there are 9 solutions to the equation $A(E) - E = 0$, the total amount of possible edge states is 18. The double degeneracy of each energy solution is, once again, a result of the emergent sublattice symmetry.

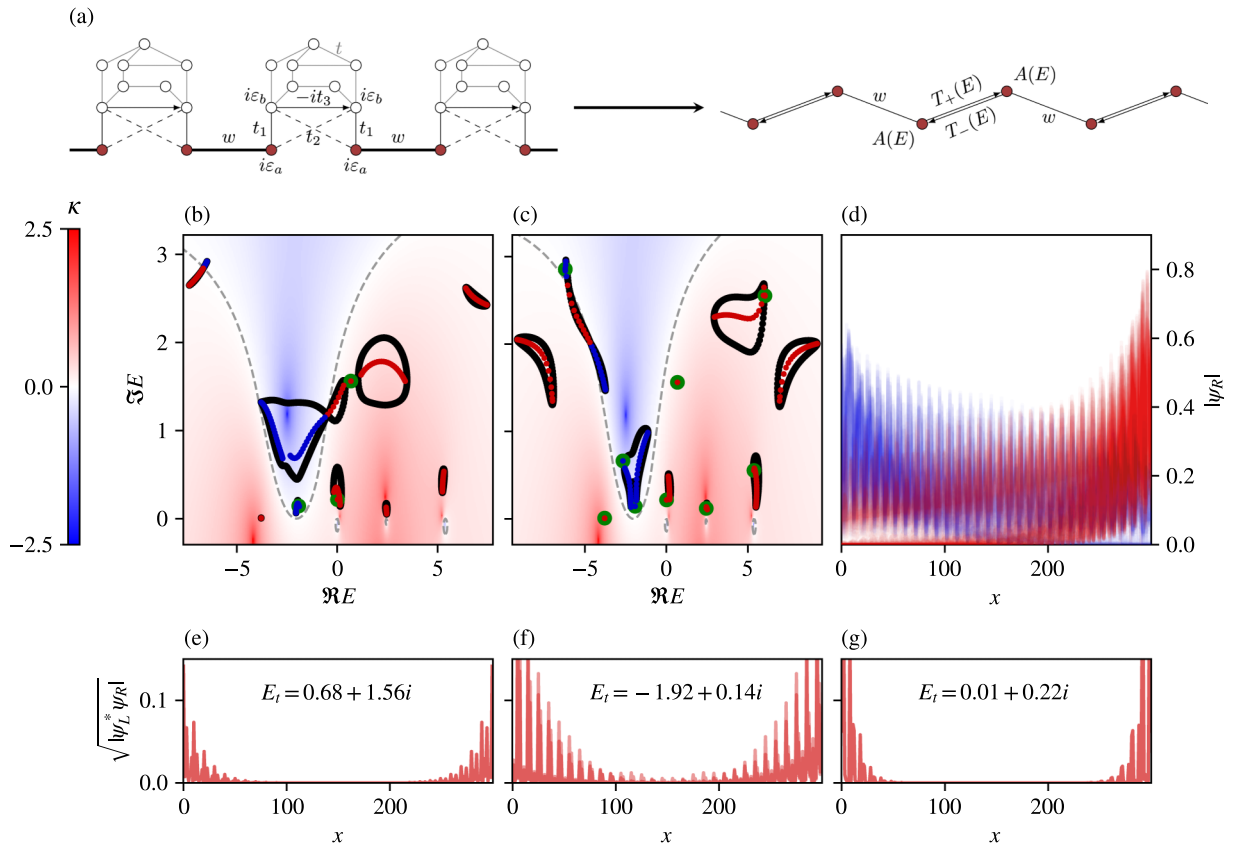


FIG. 8. Example of a generalized construction, with a network of eight sites connected to the two sites to which the ISR is applied. (a) The model and its ISR. (b) PBC (black) and OBC (right NHSE in red, left NHSE in blue) spectra of a system with the following parameters $(a, b, t_1, t_2, t_3, t, w) = (1.19, 3.74, 1.18, 2.97, 4.24, 2.03, 2.5)$, together with the three predicted edge mode energies (with double degeneracy) shown with green circles at this particular w value. Once again, the contour plot shows the skin depth $\kappa(E)$, with its values shown on the color bar in the left. (c) Same as (b), but with $w = 6.5$, where we now see all possible edge modes appear, at 9 different energies, giving a total of 18 edge modes. (d) Right-eigenstate amplitudes corresponding to the parameter choice given in (a). (e)–(g) Amplitudes of all six eigenstates (two in each figure) that appear in (a), and their corresponding energies, shown in the biorthogonal basis.

VI. CONCLUSION

Across many branches of physics, toy models are an essential tool to understand the key features of a given theory. In non-Hermitian physics, two such models are the Hatano-Nelson and the non-Hermitian Su-Schrieffer-Heeger (NH SSH) model. Despite their simple structure (their unit cells comprise only a single or two sites, respectively) these one-dimensional models host nontrivial boundary phenomena. In this work, we have used recent graph-theoretical insights to design systems whose so-called isospectral reduction, akin to an effective Hamiltonian, takes the form of either of these models. This procedure keeps the structure of the toy model, while simultaneously enriching it by making the couplings and onsite potentials energy dependent. Specifically, we have shown that this leads to *emergent Hatano-Nelson* or *emergent NH SSH models* featuring a two-sided non-Hermitian skin effect, caused by an energy dependence of the skin localization length $\kappa(E)$. This energy dependence allows different states to be localized on different ends of the system, and to have different localization strengths. For the emergent NH SSH models, we observed topological edge modes which we could further link to a quantization of the winding number. In all cases, the original system, whose isospectral reduction becomes a

Hatano-Nelson or NH SSH model, features only reciprocal (though complex-valued) couplings, with non-Hermiticity entering through complex onsite potentials (gain or loss).

We emphasize that the methods and ideas presented in this work are not limited to one-dimensional non-Hermitian Hamiltonians, but are rather generic. For example, they can be applied to higher-dimensional setups, which reduce under the isospectral reduction to paradigmatic models.

Another interesting avenue to explore would be the experimental realization of the models discussed in this work. For this endeavor, the experimental setup should be able to realize (i) gain or loss, (ii) complex-valued couplings, and (iii) different network topologies. A promising platform would be electric circuit networks, which have recently been used to implement a variety of different models, including parity-time symmetric [49] or topological systems [43,50–53]. Other possible candidates for experimental realizations are photonic or acoustic waveguides and mechanical metamaterials.

ACKNOWLEDGMENTS

A.M. and C.M.S. acknowledge the TOPCORE project with Project No. OCENW.GROOT.2019.048 which is financed

by the Dutch Research Council (NWO). L.E. and C.M.S. acknowledge the research program "Materials for the Quantum Age" (QuMat) for financial support. This program (Registration No. 024.005.006) is part of the Gravitation program financed by the Dutch Ministry of Education, Culture and Science (OCW). V.A. is supported by the EU H2020 ERC StG "NASA" Grant Agreement No. 101077954.

L.E. and A.M. contributed equally to this work.

APPENDIX A: DETAILED CALCULATIONS FOR THE NHSE AND TOPOLOGY

1. Constraints on the NHSE

As stated in the main text, the NHSE appears whenever $|T_+(E)| \neq |T_-(E)|$, where $T_{\pm}(E)$ is given by Eq. (7). From Eqs. (6) and (7), we derive the following constraint equation:

$$\frac{2t_1t_2(\varepsilon_b - E_I)[t_1^2t_3 + t_2[-t_2t_3 + t_3^2 + (\varepsilon_b - E_I)^2 + E_R^2]]}{[(\varepsilon_b - E_I)^2 + (t_3 - E_R)^2][(\varepsilon_b - E_I)^2 + (t_3 + E_R)^2]} = 0. \quad (\text{A1})$$

From this constraint equation, we can easily see that the NHSE disappears whenever $t_1 = 0$, $t_2 = 0$, or $\varepsilon_b = 0$. Equation (A1) also allows us to determine the contour curves of

$\kappa(E) = 0$, which were plotted in Figs. 2(d) and 3(d). These are given by

$$E_I = \varepsilon_b, \\ E_I = \varepsilon_b \pm \frac{\sqrt{-t_2[E_R^2t_2 + t_3(t_1^2 - t_2^2 + t_2t_3)]}}{t_2}. \quad (\text{A2})$$

2. Determining the topological transition energies of the four-band model

The constraint equation that allows us to find the topological phase transition energies is $A(E) - E = 0$. This condition yields the cubic equation

$$E^3 - i(\varepsilon_a + 2\varepsilon_b)E^2 - (t_1^2 + t_2^2 + t_3^2 + 2\varepsilon_a\varepsilon_b + \varepsilon_b^2)E + i[\varepsilon_a t_3^2 + \varepsilon_b(t_1^2 + t_2^2) + \varepsilon_a\varepsilon_b^2] = 0. \quad (\text{A3})$$

This equation can be solved exactly and the solutions are used to determine the transition energies. These are given by

$$E_1 = -\frac{1}{3}[A - 2^{\frac{1}{3}}\mathcal{F}_1 - 2^{-\frac{1}{3}}\mathcal{F}_2], \\ E_2 = -\frac{1}{3}[A + (-2)^{\frac{1}{3}}\mathcal{F}_1 - \frac{1}{2}(-2)^{\frac{2}{3}}\mathcal{F}_2], \\ E_3 = -\frac{1}{3}[A + (-1)^{\frac{2}{3}}2^{\frac{1}{3}}\mathcal{F}_1 - (-2)^{-\frac{1}{3}}\mathcal{F}_2], \quad (\text{A4})$$

where we have defined the following expressions:

$$\mathcal{F}_1 = \frac{A^2 - 3B}{[-2A^3 + 9AB - 18C + 3\sqrt{3(4B - A^2)B^2 + 6A(2A^2 - 9B)C + 81C^2}]^{\frac{1}{3}}}, \\ \mathcal{F}_2 = [-2A^3 + 9AB - 18C + 3\sqrt{3(4B - A^2)B^2 + 6A(2A^2 - 9B)C + 81C^2}]^{\frac{1}{3}},$$

with

$$A = -i\varepsilon_a + 2i\varepsilon_b, \\ B = -t_1^2 - t_2^2 - t_3^2 - 2\varepsilon_a\varepsilon_b - \varepsilon_b^2, \\ C = i\varepsilon_a t_3^2 + i\varepsilon_b(t_1^2 + t_2^2) + i\varepsilon_a\varepsilon_b^2.$$

3. The 10-band model

The Bloch Hamiltonian for the 10-band model shown in Fig. 8 is given by

$$H(k) = \begin{pmatrix} i\varepsilon_a & 0 & 0 & t_1 & t_2 & 0 & 0 & 0 & 0 & we^{-ik} \\ 0 & 0 & 0 & 0 & t & 0 & t & 0 & 0 & 0 \\ 0 & 0 & 0 & 0 & 0 & t & t & t & 0 & 0 \\ t_1 & 0 & 0 & i\varepsilon_b & -it_3 & 0 & t & 0 & t & t_2 \\ t_2 & t & 0 & it_3 & i\varepsilon_b & 0 & 0 & t & 0 & t_1 \\ 0 & 0 & t & 0 & 0 & 0 & 0 & t & t & 0 \\ 0 & t & t & t & 0 & 0 & 0 & 0 & 0 & 0 \\ 0 & 0 & t & 0 & t & t & 0 & 0 & t & 0 \\ 0 & 0 & 0 & t & 0 & t & 0 & t & 0 & 0 \\ we^{ik} & 0 & 0 & t_2 & t_1 & 0 & 0 & 0 & 0 & i\varepsilon_a \end{pmatrix}.$$

Upon performing the ISR, the energy-dependent onsite term $A(E)$ and hopping parameters $T_{\pm}(E) \equiv v(E) \pm g(E)$ are

given by

$$A(E) = i\varepsilon_a + \frac{\sum_{n=0}^7 c_n E^n}{\sum_{m=1}^8 d_m E^m}, \\ v(E) = \frac{\sum_{n=0}^7 p_n E^n}{\sum_{m=1}^8 d_m E^m}, \\ g(E) = \frac{\sum_{n=0}^7 q_n E^n}{\sum_{m=1}^8 d_m E^m}. \quad (\text{A5})$$

The coefficients of the polynomials can be found in Table I. They provide all the necessary ingredients to numerically solve for the nine energies that satisfy the equation $A(E) - E = 0$, and at which the topological edge modes appear.

4. Quantization of the winding number

The winding number for the reduced model in Sec. IV is given by Eq. (13). Working out the trace of the product of matrices yields the following equation:

$$\mathcal{W}(E_t) = \int_{-\pi}^{\pi} \frac{dk}{2\pi i} \frac{ie^{ik}w[w + a(E_t)\cos k]}{[e^{ik}a(E_t) + w][(a(E_t) + e^{ik}w)]},$$

TABLE I. Polynomial coefficients for $A(E)$, $v(E)$, and $g(E)$.

n	c_n	p_n	q_n	d_n
0	$-2t^7(t_1 - t_2)^2$	$2t^7(t_1 - t_2)^2$	0	$4t^7(2t + i\varepsilon_b)$
1	$-2t^5[4t(t_1^2 + t_1t_2 + t_2^2) + 3i\varepsilon_b(t_1^2 + t_2^2)]$	$-4t^5[t(t_1^2 + 4t_1t_2 + t_2^2) + 3i\varepsilon_bt_1t_2]$	$-6it^5t_3(t_1^2 - t_2^2)$	$-2t^5(3\varepsilon_b^2 - 8i\varepsilon_bt + 2t^2 + 3t_3^2)$
2	$4t^4[t(2t_1^2 - 3t_1t_2 + 2t_2^2) - 2i\varepsilon_b(t_1^2 + t_2^2)]$	$-2t^4[t(3t_1^2 - 8t_1t_2 + 3t_2^2) + 8i\varepsilon_bt_1t_2]$	$-8it^4t_3(t_1^2 - t_2^2)$	$-8t^4(\varepsilon_b^2 + 2i\varepsilon_bt + 4t^2 + t_3^2)$
3	$2t^3[t(9t_1^2 + 2t_1t_2 + 9t_2^2) + 2i\varepsilon_b(t_1^2 + t_2^2)]$	$2t^3[t(t_1^2 + 18t_1t_2 + t_2^2) + 4i\varepsilon_bt_1t_2]$	$4it^3t_3(t_1^2 - t_2^2)$	$2t^3(2\varepsilon_b^2 - 18i\varepsilon_bt + 5t^2 + 2t_3^2)$
4	$t^2[-4t(t_1^2 - t_1t_2 + t_2^2) + 7i\varepsilon_b(t_1^2 + t_2^2)]$	$2t^2[t(t_1^2 - 4t_1t_2 + t_2^2) + 7i\varepsilon_bt_1t_2]$	$7it^2t_3(t_1^2 - t_2^2)$	$t^2(7\varepsilon_b^2 + 8i\varepsilon_bt + 32t^2 + 7t_3^2)$
5	$-9t^2(t_1^2 + t_2^2)$	$-18t^2t_1t_2$	0	$2t^2(-2t + 9i\varepsilon_b)$
6	$-i\varepsilon_b(t_1^2 + t_2^2)$	$-2i\varepsilon_bt_1t_2$	$-it_3(t_1^2 - t_2^2)$	$-\varepsilon_b^2 - 11t^2 - t_3^2$
7	$t_1^2 + t_2^2$	$2t_1t_2$	0	$-2i\varepsilon_b$
8	0	0	0	1

where $a(E_t) = \sqrt{v^2(E_t) - g^2(E_t)}$. We can turn this into a contour integral on the unit circle S^1 by letting $z = e^{ik}$. This gives

$$\begin{aligned} \mathcal{W}(E_t) &= \oint_{S^1} \frac{dz}{2\pi i} \frac{1}{2} \frac{w[2w + a(z + \frac{1}{z})]}{(za + w)(a + zw)}, \\ &= \oint_{S^1} \frac{dz}{2\pi i} \frac{1}{2a} \frac{2wz + a(z^2 + 1)}{z(z + \frac{a}{w})(z + \frac{w}{a})}, \\ &\equiv \oint_{S^1} \frac{dz}{2\pi i} f(z), \end{aligned}$$

where we omitted the argument E_t in a , for brevity. The function $f(z)$ has two poles inside the unit circle and one outside. The pole $z_0 = 0$ is always inside, while $z_1 = w/a$ is inside if $|w| < |a|$ (making $z_2 = a/w$ outside). Using the residue theorem, we then have the following conditions:

$$\mathcal{W}(E_t) = \begin{cases} \text{Res}(f, z_0) + \text{Res}(f, z_1), & \text{if } |w| < |a(E_t)| \\ \text{Res}(f, z_0) + \text{Res}(f, z_2), & \text{if } |w| > |a(E_t)|. \end{cases}$$

Since the poles are of order 1, the residues are simply given by

$$\begin{aligned} \text{Res}(f, z_0) &= \lim_{z \rightarrow z_0} (z - z_0)f(z) = \frac{1}{2}, \\ \text{Res}(f, z_1) &= \lim_{z \rightarrow z_1} (z - z_1)f(z) = -\frac{1}{2}, \\ \text{Res}(f, z_2) &= \lim_{z \rightarrow z_2} (z - z_2)f(z) = \frac{1}{2}, \end{aligned}$$

which finishes the proof of the quantization of the winding number,

$$\mathcal{W}(E_t) = \begin{cases} 0, & \text{if } |w| < \sqrt{|v^2(E_t) - g^2(E_t)|} \\ 1, & \text{if } |w| > \sqrt{|v^2(E_t) - g^2(E_t)|}. \end{cases}$$

APPENDIX B: TOPOLOGICAL PHASE TRANSITIONS IN THE EMERGENT NH SSH MODEL

In this Appendix, we analyze the different topological phases of the model described by Eq. (10), which reduces to the NH SSH model. Figure 9(a) shows the absolute value of the spectrum as a function of w for OBC. Here, one can observe the emergence of edge modes for different values of w . The topological nature of these modes is further elaborated

upon in the main text. We then take ‘‘slices’’ of Fig. 9(a) at fixed w to obtain Figs. 9(b)–9(f), where both OBC (red) and PBC (black) spectra are shown in the complex plane. The chosen values of w correspond to the vertical dashed lines in Fig. 9(a). Figures 9(b), 9(d), and 9(f) show a trivial phase and two distinct topological phases, respectively. Figures 9(c) and 9(e) show the two (OBC) line-gap closings. It should be noted that, due to the breakdown of the bulk-boundary correspondence for non-Hermitian systems, the line-gap closings for OBC and PBC do not take place at the same point in parameter space.

APPENDIX C: ADDITIONAL INFORMATION FOR CONSTRUCTION PRINCIPLES

In the following, we show why the ISR of the structure depicted in Fig. 5(a) has the structure

$$\mathcal{R}_S(E, H) = \begin{pmatrix} A(E)/2 & T_+(E) \\ T_-(E) & A(E)/2 \end{pmatrix}.$$

To show this statement, we note that there exists a block-diagonal matrix Q such that $HQ = QH^T$, with

$$Q = \begin{pmatrix} 0 & e^{i\phi} \\ e^{i\phi} & 0 \end{pmatrix} \oplus I \equiv X \oplus I,$$

where we have enumerated the sites such that the two red sites u, v are sites 1 and 2. Writing $HQ = QH^T$ in block form gives us the important relations

$$XH_{S,S} = (H_{S,S})^T X, \quad (C1)$$

$$XH_{S,\bar{S}} = (H_{\bar{S},S})^T, \quad (C2)$$

$$H_{\bar{S},S} = (H_{S,\bar{S}})^T X, \quad (C3)$$

$$H_{\bar{S},\bar{S}} = (H_{\bar{S},\bar{S}})^T. \quad (C4)$$

Equipped with these insights, we proceed by noting that the ISR over S can be written as (see Lemma 4 in the

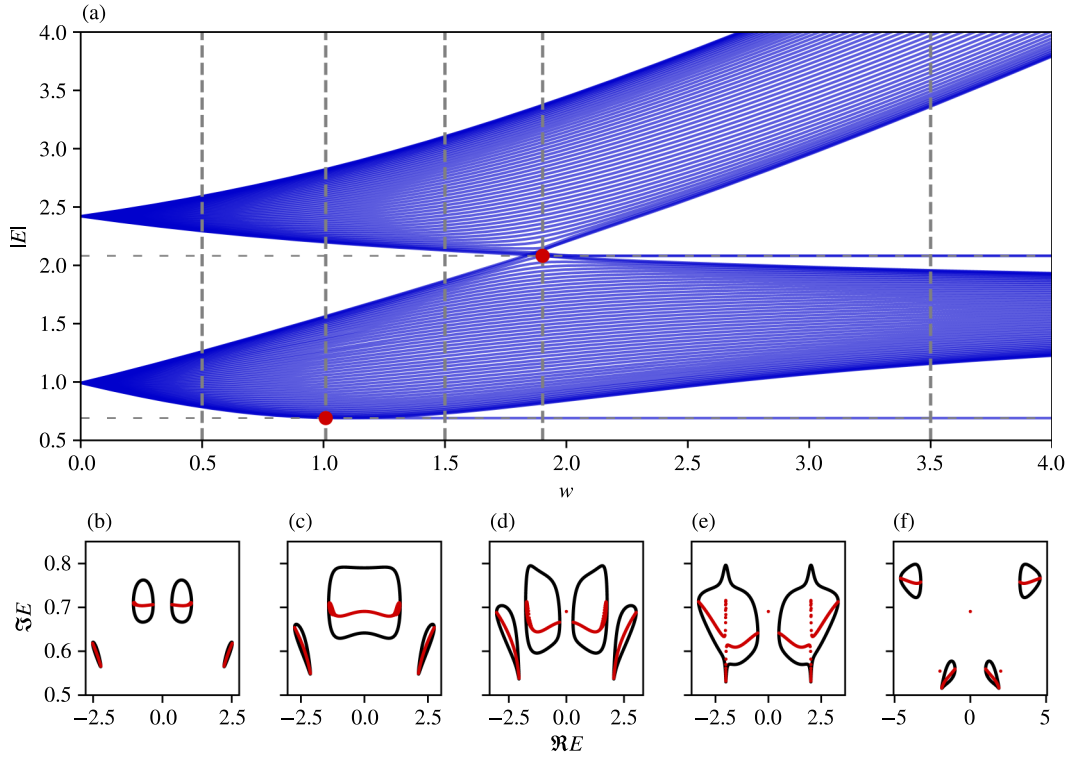


FIG. 9. Behavior of the band structure (absolute value) of the emergent NH SSH model as described in Sec. IV. (a) Absolute value of the spectrum for $(\varepsilon_a, \varepsilon_b, t_1, t_2, t_3) = (0.8, 0.5, 1, 0.7, 1.6)$ as a function of w , for OBC with $N = 50$ unit cells. There are three topologically distinct phases. The transitions are denoted by a red dot, sitting at the intersection between the edge modes' energies (horizontal dashed gray line) and the critical w values. (b)–(f) The spectrum in the complex plane for fixed w corresponding to the vertical dashed gray lines in (a). Red and black points denote the OBC and PBC spectra, respectively. (b) Trivial phase, (c) first line-gap closing, (d) topological phase with one (degenerate) pair of edge modes, (e) second line-gap closing, (f) topological phase with three (degenerate) pairs of edge modes.

Supplemental Material of Ref. [37])

$$\mathcal{R}_S(E, H) = H_{S,S} + \sum_{k=0}^{|\bar{S}|-1} a_k H_{S,\bar{S}} (H_{\bar{S},\bar{S}} - EI)^{k-1} H_{\bar{S},S}, \quad (\text{C5})$$

where $|\bar{S}|$ denotes the number of sites in \bar{S} , and with E -dependent coefficients a_k that are obtained from the characteristic polynomial of $H_{\bar{S},\bar{S}} - EI$. Now, using (C1) to (C4) and defining $Y \equiv H_{\bar{S},\bar{S}} - EI$, we obtain

$$X \mathcal{R}_S(E, H) X^{-1} \quad (\text{C6})$$

$$= X H_{S,S} X^{-1} + \sum_{k=0}^{|\bar{S}|} a_k X H_{S,\bar{S}} Y^{k-1} H_{\bar{S},S} X^{-1} \quad (\text{C7})$$

$$= (H_{S,S})^T + \sum_{k=0}^{|\bar{S}|} a_k (H_{S,\bar{S}})^T (Y^{k-1})^T (H_{\bar{S},S})^T \quad (\text{C8})$$

$$= [\mathcal{R}_S(E, H)]^T, \quad (\text{C9})$$

where we have used that $H_{\bar{S},\bar{S}}$ is symmetric. From comparing the first and last equations, it follows that the two sites of the effective Hamiltonian must have the same energy-dependent onsite potential $A(E)/2$, while the couplings T_{\pm} between them are, in general, different from each other.

- [1] A. McDonald and A. A. Clerk, Exponentially-enhanced quantum sensing with non-Hermitian lattice dynamics, *Nat. Commun.* **11**, 5382 (2020).
- [2] P. San-Jose, J. Cayao, E. Prada, and R. Aguado, Majorana bound states from exceptional points in non-topological superconductors, *Sci. Rep.* **6**, 21427 (2016).
- [3] A. Ghatak, M. Brandenbourger, J. van Wezel, and C. Coulais, Observation of non-Hermitian topology and its bulk-edge correspondence in an active mechanical metamaterial, *Proc. Natl. Acad. Sci. USA* **117**, 29561 (2020).

- [4] K. Sone, Y. Ashida, and T. Sagawa, Exceptional non-Hermitian topological edge mode and its application to active matter, *Nat. Commun.* **11**, 5745 (2020).
- [5] F. K. Kunst, E. Edvardsson, J. C. Budich, and E. J. Bergholtz, Biorthogonal bulk-boundary correspondence in non-Hermitian systems, *Phys. Rev. Lett.* **121**, 026808 (2018).
- [6] E. J. Bergholtz, J. C. Budich, and F. K. Kunst, Exceptional topology of non-Hermitian systems, *Rev. Mod. Phys.* **93**, 015005 (2021).

- [7] K. Kawabata, K. Shiozaki, M. Ueda, and M. Sato, Symmetry and topology in non-Hermitian physics, *Phys. Rev. X* **9**, 041015 (2019).
- [8] Z. Gong, Y. Ashida, K. Kawabata, K. Takasan, S. Higashikawa, and M. Ueda, Topological phases of non-Hermitian systems, *Phys. Rev. X* **8**, 031079 (2018).
- [9] T. E. Lee, Anomalous edge state in a non-Hermitian lattice, *Phys. Rev. Lett.* **116**, 133903 (2016).
- [10] S. Yao and Z. Wang, Edge states and topological invariants of non-Hermitian systems, *Phys. Rev. Lett.* **121**, 086803 (2018).
- [11] N. Okuma, K. Kawabata, K. Shiozaki, and M. Sato, Topological origin of non-Hermitian skin effects, *Phys. Rev. Lett.* **124**, 086801 (2020).
- [12] L. Zhang, Y. Yang, Y. Ge, Y.-J. Guan, Q. Chen, Q. Yan, F. Chen, R. Xi, Y. Li, D. Jia, S.-Q. Yuan, H.-X. Sun, H. Chen, and B. Zhang, Acoustic non-Hermitian skin effect from twisted winding topology, *Nat. Commun.* **12**, 6297 (2021).
- [13] S. Liu, R. Shao, S. Ma, L. Zhang, O. You, H. Wu, Y. J. Xiang, T. J. Cui, and S. Zhang, Non-Hermitian skin effect in a non-Hermitian electrical circuit, *Research* **2021**, 5608038 (2021).
- [14] Z. Gu, H. Gao, H. Xue, J. Li, Z. Su, and J. Zhu, Transient non-Hermitian skin effect, *Nat. Commun.* **13**, 7668 (2022).
- [15] Q. Liang, D. Xie, Z. Dong, H. Li, H. Li, B. Gadway, W. Yi, and B. Yan, Dynamic signatures of non-Hermitian skin effect and topology in ultracold atoms, *Phys. Rev. Lett.* **129**, 070401 (2022).
- [16] M. A. Bandres and M. Segev, non-Hermitian topological systems, *Physics* **11**, 96 (2018).
- [17] F. K. Kunst and V. Dwivedi, Non-Hermitian systems and topology: A transfer-matrix perspective, *Phys. Rev. B* **99**, 245116 (2019).
- [18] L. Li, C. H. Lee, and J. Gong, Topological switch for non-Hermitian skin effect in cold-atom systems with loss, *Phys. Rev. Lett.* **124**, 250402 (2020).
- [19] A. Altland and M. R. Zirnbauer, Nonstandard symmetry classes in mesoscopic normal-superconducting hybrid structures, *Phys. Rev. B* **55**, 1142 (1997).
- [20] Z. Yang, K. Zhang, C. Fang, and J. Hu, non-Hermitian bulk-boundary correspondence and auxiliary generalized Brillouin zone theory, *Phys. Rev. Lett.* **125**, 226402 (2020).
- [21] N. Hatano and D. R. Nelson, Vortex pinning and non-Hermitian quantum mechanics, *Phys. Rev. B* **56**, 8651 (1997).
- [22] W. P. Su, J. R. Schrieffer, and A. J. Heeger, Solitons in polyacetylene, *Phys. Rev. Lett.* **42**, 1698 (1979).
- [23] S. Lieu, Topological phases in the non-Hermitian Su-Schrieffer-Heeger model, *Phys. Rev. B* **97**, 045106 (2018).
- [24] L. Bunimovich and B. Webb, *Isospectral Transformations: A New Approach to Analyzing Multidimensional Systems and Networks*, 1st ed., Springer Monographs in Mathematics (Springer, New York, 2014).
- [25] L. Bunimovich, D. Smith, and B. Webb, Finding hidden structures, hierarchies, and cores in networks via isospectral reduction, *Appl. Math. Nonlinear Sci.* **4**, 231 (2019).
- [26] L. A. Bunimovich and B. Z. Webb, Isospectral graph reductions and improved estimates of matrices' spectra, *Linear Algebra Its Appl.* **437**, 1429 (2012).
- [27] F. G. Vasquez and B. Z. Webb, Pseudospectra of isospectrally reduced matrices, *Numer. Linear Algebra Appl.* **22**, 145 (2014).
- [28] L. Brillouin, Les problèmes de perturbations et les champs self-consistents, *J. Phys. Radium* **3**, 373 (1932).
- [29] J. Hubbard, Calculation of partition functions, *Phys. Rev. Lett.* **3**, 77 (1959).
- [30] D. Chruściński and A. Kossakowski, Feshbach projection formalism for open quantum systems, *Phys. Rev. Lett.* **111**, 050402 (2013).
- [31] D. Smith and B. Webb, Hidden symmetries in real and theoretical networks, *Phys. A (Amsterdam)* **514**, 855 (2019).
- [32] M. Kempton, J. Sinkovic, D. Smith, and B. Webb, Characterizing cospectral vertices via isospectral reduction, *Linear Algebra Its Appl.* **594**, 226 (2020).
- [33] A. J. Schwenk, Almost all trees are cospectral, in *Proceedings of the Third Annual Arbor Conference* (Academic, New York, 1973), pp. 257–307.
- [34] C. Godsil and J. Smith, Strongly cospectral vertices, [arXiv:1709.07975](https://arxiv.org/abs/1709.07975).
- [35] M. Röntgen, N. E. Palaiodimopoulos, C. V. Morfonios, I. Brouzos, M. Pyzh, F. K. Diakonov, and P. Schmelcher, Designing pretty good state transfer via isospectral reductions, *Phys. Rev. A* **101**, 042304 (2020).
- [36] C. V. Morfonios, M. Röntgen, M. Pyzh, and P. Schmelcher, Flat bands by latent symmetry, *Phys. Rev. B* **104**, 035105 (2021).
- [37] M. Röntgen, M. Pyzh, C. V. Morfonios, N. E. Palaiodimopoulos, F. K. Diakonov, and P. Schmelcher, Latent symmetry induced degeneracies, *Phys. Rev. Lett.* **126**, 180601 (2021).
- [38] M. Röntgen, C. V. Morfonios, P. Schmelcher, and V. Pagneux, Hidden symmetries in acoustic wave systems, *Phys. Rev. Lett.* **130**, 077201 (2023).
- [39] M. Röntgen, O. Richoux, G. Theocharis, C. V. Morfonios, P. Schmelcher, P. del Hougne, and V. Achilleos, Equireflectionality and customized unbalanced coherent perfect absorption in asymmetric waveguide networks, [arXiv:2305.02786](https://arxiv.org/abs/2305.02786).
- [40] J. Sol, M. Röntgen, and P. del Hougne, Covert scattering control in metamaterials with non-locally encoded hidden symmetry, *Adv. Mater.* **2303891**, doi:10.1002/adma.202303891.
- [41] Z. Lin, L. Ding, S. Ke, and X. Li, Steering non-Hermitian skin modes by synthetic gauge fields in optical ring resonators, *Opt. Lett.* **46**, 3512 (2021).
- [42] H. Xin, W. Song, S. Wu, Z. Lin, S. Zhu, and T. Li, Manipulating the non-Hermitian skin effect in optical ring resonators, *Phys. Rev. B* **107**, 165401 (2023).
- [43] M. Röntgen, X. Chen, W. Gao, M. Pyzh, P. Schmelcher, V. Pagneux, V. Achilleos, and A. Coutant, Latent Su-Schrieffer-Heeger models, [arXiv:2310.07619](https://arxiv.org/abs/2310.07619).
- [44] M. Röntgen, Latent Symmetries: An Introduction, Other, MetaMAT Weekly Seminars, 2022 (unpublished).
- [45] A. A. Clerk, Introduction to quantum non-reciprocal interactions: from non-Hermitian Hamiltonians to quantum master equations and quantum feedforward schemes, *SciPost Phys. Lect. Notes*, **44** (2022).
- [46] F. Song, S. Yao, and Z. Wang, Non-Hermitian topological invariants in real space, *Phys. Rev. Lett.* **123**, 246801 (2019).
- [47] M. Creutz, End states, ladder compounds, and domain-wall fermions, *Phys. Rev. Lett.* **83**, 2636 (1999).
- [48] C. V. Morfonios, M. Pyzh, M. Röntgen, and P. Schmelcher, Cospectrality preserving graph modifications and eigenvector properties via walk equivalence of vertices, *Linear Algebra Its Appl.* **624**, 53 (2021).
- [49] S. Liu, S. Ma, C. Yang, L. Zhang, W. Gao, Y. J. Xiang, T. J. Cui, and S. Zhang, Gain- and loss-induced topological insulating

- phase in a non-Hermitian electrical circuit, [Phys. Rev. Appl. **13**, 014047 \(2020\)](#).
- [50] J. Dong, V. Juričić, and B. Roy, Topoelectric circuits: Theory and construction, [Phys. Rev. Res. **3**, 023056 \(2021\)](#).
- [51] S. Liu, S. Ma, Q. Zhang, L. Zhang, C. Yang, O. You, W. Gao, Y. Xiang, T. J. Cui, and S. Zhang, Octupole corner state in a three-dimensional topological circuit, [Light Sci. Appl. **9**, 145 \(2020\)](#).
- [52] C. H. Lee, S. Imhof, C. Berger, F. Bayer, J. Brehm, L. W. Molenkamp, T. Kiessling, and R. Thomale, Topoelectrical circuits, [Commun. Phys. **1**, 39 \(2018\)](#).
- [53] S. Imhof, C. Berger, F. Bayer, J. Brehm, L. W. Molenkamp, T. Kiessling, F. Schindler, C. H. Lee, M. Greiter, T. Neupert, and R. Thomale, Topoelectrical-circuit realization of topological corner modes, [Nat. Phys. **14**, 925 \(2018\)](#).